Design and fabrication of plasmonic cavities for magneto-optical sensing

Design and fabrication of plasmonic cavities for magneto-optical sensing

T. H. J. Loughran, J. Roth, P. S. Keatley, E. Hendry, W. L. Barnes, R. J. Hicken, J. F. Einsle, A. Amy, W. Hendren, R. M. Bowman, and P. Dawson

Citation: AIP Advances **8**, 055207 (2018); doi: 10.1063/1.5021538
View online: https://doi.org/10.1063/1.5021538
View Table of Contents: http://aip.scitation.org/toc/adv/8/5
Published by the American Institute of Physics

Design and fabrication of plasmonic cavities for magneto-optical sensing

T. H. J. Loughran,[1,a] J. Roth,[1] P. S. Keatley,[1] E. Hendry,[1] W. L. Barnes,[1] R. J. Hicken,[1] J. F. Einsle,[2] A. Amy,[2] W. Hendren,[2] R. M. Bowman,[2] and P. Dawson[2]

[1]*University of Exeter, Department of Physics and Astronomy, Exeter EX4 4QL, United Kingdom*
[2]*Queen's University Belfast, School of Mathematics and Physics, Center for Nanostructured Media, Belfast BT7 1NN, United Kingdom*

(Received 5 January 2018; accepted 25 April 2018; published online 8 May 2018)

The design and fabrication of a novel plasmonic cavity, intended to allow far-field recovery of signals arising from near field magneto-optical interactions, is presented. Finite element modeling is used to describe the interaction between a gold film, containing cross-shaped cavities, with a nearby magnetic under-layer. The modeling revealed strong electric field confinement near the center of the cross structure for certain optical wavelengths, which may be tuned by varying the length of the cross through a range that is compatible with available fabrication techniques. Furthermore, the magneto optical Kerr effect (MOKE) response of the composite structure can be enhanced with respect to that of the bare magnetic film. To confirm these findings, cavities were milled within gold films deposited upon a soluble film, allowing relocation to a ferromagnetic film using a float transfer technique. Cross cavity arrays were fabricated and characterized by optical transmission spectroscopy prior to floating, revealing resonances at optical wavelengths in good agreement with the finite element modeling. Following transfer to the magnetic film, circular test apertures within the gold film yielded clear magneto-optical signals even for diameters within the sub-wavelength regime. However, no magneto-optical signal was observed for the cross cavity arrays, since the FIB milling process was found to produce nanotube structures within the soluble under-layer that adhered to the gold. Further optimization of the fabrication process should allow recovery of magneto-optical signal from cross cavity structures. https://doi.org/10.1063/1.5021538

INTRODUCTION

As magnetic hard disk drive capacities increase and the realisation of practical spintronic devices is demonstrated,[1,2] there is an urgent need to observe dynamic magnetic phenomena with increased spatial resolution. Measurement techniques such as magnetic force microscopy deliver excellent spatial resolution, but the addition of sub-ns temporal resolution is non-trivial. Time resolved X-ray measurement techniques have been demonstrated that exploit x-ray magnetic circular dichroism (XMCD).[3,4] Deep nanoscale spatial resolution can be obtained in wide-field or scanning transmission measurements, or else XMCD can be combined with the imaging capability of photoemission electron microscopy (PEEM),[5] or holography techniques.[6] While extremely powerful, x-ray measurements require the use of synchrotron radiation and are not routinely available.

Time resolved scanning Kerr microscopy (TRSKM), is a powerful technique for characterising magnetisation dynamics[7–9] down to sub-ps timescales. While spatial resolution is currently determined by the optical diffraction limit, any improvement could yield a powerful table-top probe

[a]Electronic mail: T.H.J.Loughran@exeter.ac.uk

of nanoscale structures. A platform for time resolved magneto-optical (MO) measurements in the near field has recently been demonstrated.[10] This platform makes use of an aperture defined within the gold coating of a dielectric AFM tip, and spatial resolution slightly better than the diffraction limit has been demonstrated using a circular aperture. There is now great interest in improving the spatial resolution through optimization of the aperture structure and exploitation of plasmonic effects. Previous work in the field of plasmonics has demonstrated localisation of electro-magnetic fields to sub-wavelength regions by suitably designed structures.[11–15]

Much of the work on combined magnetic plasmonic systems has involved driving plasmons in magnetic media.[16–19] However it has previously been shown that MO effects can be enhanced by bringing established plasmonic materials into close proximity with magneto-optically active materials, whether by coating magnetic particles with gold,[20] creating combined nano-particles of gold and cobalt,[21] or by suspending gold nano-particles above $Au/Co/Au$ multi-layers with a dielectric spacer.[22]

A suitable plasmonic MO probe requires a structure that is able to couple to orthogonal polarization states so that polarization conversion may be observed. That is to say the structure must both couple to the incident polarization state of the light, and be capable of coupling out an orthogonal polarization state that is induced by MO interaction within the sample. In addition it is desirable for a probe to exhibit high spatial confinement of the electric field (leading to increased spatial resolution), and enhanced MO signal in order to compensate for signal loss due to the smaller area of interaction. By combining two cavities of orthogonal orientation, a cross cavity structure is able to enhance the electric field in a small region at the center of the cross, while interacting with orthogonal polarization states with similar efficiency. In the present paper, the response of realistic cross apertures is modeled, and attempts to fabricate and characterize such structures are reported. Moreover, using finite element modeling, it can be shown that such a structure allows penetration of the electric field into magnetic under layers, making it an ideal near field probe for TRSKM of ferromagnetic layers.

MODELING

A finite element modelling approach was used to assess the optical properties of cross-shaped cavity structures, and to explore the influence of different geometrical parameters. Finite element modelling was performed in "COMSOL^{TM}Multiphysics" (from hereon referred to as "COMSOL"), utilising a similar geometry and modelling method to that outlined in more detail previously.[23] Each structure was defined within the unit cell of an infinite periodic array, with appropriate periodic boundary conditions. The model is periodic for computational simplicity and the unit cell width is chosen to be as small as possible (350nm) in order to limit the appearance of features associated with the period of the array, since the response of an individual cavity is of primary interest here. The unit cell typically consisted of a gold structure separated from a magnetic layer by a dielectric spacer layer. In the absence of the gold the modelled structure reduces to an optically thick slab of ferromagnetic material coated with a dielectric layer. The MO properties of the magnetic film were chosen to mimic those of permalloy at 800 nm incident wavelength, so as to predict the order of magnitude response for typical TRSKM experiments, rather than to reproduce the experimental results described later in the present work. The magnetization was defined to lie normal to the plane of the film (parallel to the $\hat{z}$ axis). The magneto-optical effects arise from off-diagonal terms in the permittivity tensor,[24,25] with values of the MO constant taken from the literature.[26] The choice of a wavelength independent magnetic permittivity allows the spectral response of the gold structure to be separated from that of the magnetic material. This allows the plasmonic structure to optimised independently of the magnetic material used, so that a sample independent probe may be fabricated. The wavelength dependent permittivity of the gold was obtained by interpolation of published values.[27] Here the gold permittivity is treated as isotropic, and lacks the MO terms that have been reported in some studies[28] because only the MO response generated by the magnetic layer is relevant for the intended application to TRSKM.

A schematic of the modeled structure is shown in Figure 1. A plane wave is incident on a gold structure propagating from the air side at normal incidence. The magnetization is defined as lying along the long axis of the model in the negative $\hat{z}$ direction, so as to generate a polar Kerr effect.

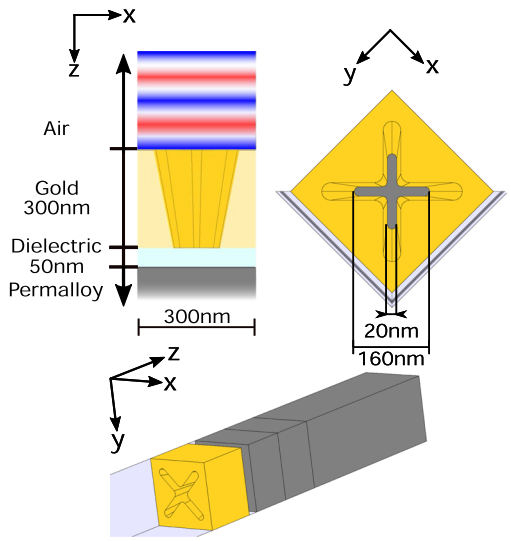

FIG. 1. Schematic of the unit cell used in finite element modeling, showing some typical length scales. A gold layer is separated from a ferromagnetic layer by a thin dielectric region. The gold layer has a cross shape removed from it, with sloping walls and filleting to produce a more realistic cross profile. The slope is achieved by scaling the cross in the $\hat{x}$ and $\hat{y}$ directions, while extruding the shape in the $\hat{z}$ direction. The stated arm lengths correspond to the dimensions of the cross at the dielectric interface, since these dimensions are more easily controlled. A plane wave with polarization along the $\hat{x}$ direction propagates in the positive $\hat{z}$ direction from the air side of the model.

The cavity has the form of a modified cut-cross cavity resonator i.e. a planar gold film with a symmetric cross shape removed. The four-fold symmetry of the structure is chosen so that orthogonal optical polarization states may be absorbed and re-radiated with similar efficiency, which is essential for detection of the MOKE, which is a form of circular birefringence/dichroism that induces polarization conversion when the incident light is plane polarized. In addition, the length of the cross arms can be varied to achieve resonance at different wavelengths, allowing the cavity to be tuned to the laser wavelength in experiments. The structures modeled here are intended to resemble those that may be realized with the fabrication techniques available. Therefore the cavity has sloping walls and filleting (smoothing) of the corners, mimicking the unavoidable slope ($\approx 15^\circ$) and finite patterning sharpness inherent in fabrication by focused ion beam (FIB) milling. The correct slope is achieved by introducing an in plane scaling factor that is applied during extrusion (extension of a 2D shape through a 3rd dimension to create a solid object) of a planar cross shape. In addition, the cross arms were chosen to be 20 nm in width, reflecting the typical patterning resolution of the FIB system at practical patterning currents. The gold thickness of 300 nm and dielectric spacer thickness of 50 nm, correspond to the thicknesses of the layers in fabricated structures presented below. The dielectric material is assumed to have a relative permittivity of 2. The calculated complex relative electric field components are extracted from a slice through the air region of the model, allowing recovery of MOKE induced rotation and ellipticity. The relative electric field consists of the total electric field with the incident field subtracted, and can therefore be thought of as corresponding to the reflected electric field.

Figure 2(a) shows the wavelength dependence of the extracted absolute MOKE signal (the rotation and ellipticity signals combined in quadrature) for a range of cross lengths, as well as for the magnetic film alone with no gold structure. The rotation and ellipticity were calculated from the relative E_y and E_x components shown in Figures 2(b) and 2(c) respectively. In general the presence of a cavity produces a wavelength dependent enhancement of the total Kerr signal. For all cross lengths other than 180 nm, the signal at resonance is seen to be larger than that for the magnetic film in the absence of the gold layer. Examining the extracted peak frequencies (Figure 3) three sets of peaks can be seen. The lowest wavelength peak exhibits a smaller amplitude than the others and its position has only a weak dependence upon the arm length, suggesting that it is associated with confinement within the thickness of the gold film. At longer wavelengths it appears that there are

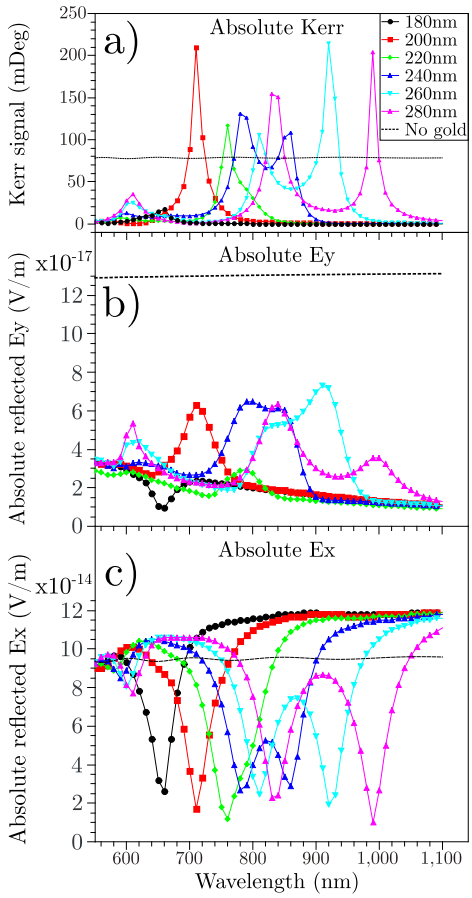

FIG. 2. a) Absolute Kerr signal (the rotation and ellipticity summed in quadrature) spectra for a series of cross structures of different arm length. The resonant wavelength varies linearly with arm length through the range studied. The maximum MOKE signal exceeds that of the bare magnetic film in all cases, and is greatest for the 200 nm arm length. The stated arm lengths are for the underside of the cross structure that faces the magnetic material. b) The spectra of the absolute relative *y* component of the electric field for a range of cross lengths, as well as the bare magnetic film (dashed line). c) The spectra of the absolute relative *x* component of the electric field.

two regimes, with the spectra for the 240 to 280 nm arm length models exhibiting three resonances. Devices with shorter arms have a dominant peak with a linear relationship between arm length and resonant wavelength. A shift then occurs at around 240 nm arm length, and the resonant wavelength shifts to longer wavelength.

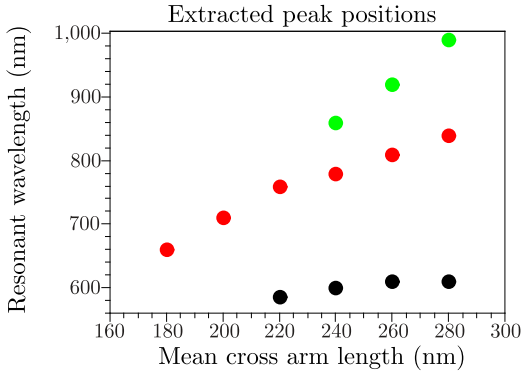

FIG. 3. Extracted peak positions for all cross arm lengths. Black, red and green symbols are used to indicate peaks in order of increasing wavelength for spectra with multiple peaks.

Figure 4 shows the field distribution for the 260 nm arm length model at the three resonant wavelengths. For the the middle wavelength resonance the electric field is strongly localized near the center of the cross on the dielectric side, where the magnetic layer is located, and its amplitude is enhanced in this region. This strong confinement makes the structure suitable as a potential imaging probe. In fact the largest field amplitude occurs at the corner edges of the cross where the arms intersect, where the geometry is most sensitive to the details of the milling technique. However if the field in this region could be practically realized, it might be of interest for high sensitivity particle measurement applications.[18,29]

However for practical applications, the absolute Kerr signal may not be the most appropriate figure of merit. Mansuripur[30] suggests that the absolute value of the component of the electric field orthogonal to the incident field, in this case "E_y", is more relevant to the measured signal level. In Figure 2(b) the absolute y component of the relative electric field is plotted, for both the full range of crosses, and the bare magnetic film. Using this figure of merit, the enhancement of the absolute Kerr signal can be seen to correspond to a more modest resonance in the E_y component. Figure 2(c) shows the absolute x component of the relative electric field. The increase in the absolute MOKE signal, is seen to be due to a combination of the resonant peak in the observed y component, and a corresponding dip in the x component, of the reflected electric field. While the value of E_y for cross cavities is reduced compared to the bare film, it is still larger than one might expect given the reduced region of interaction between the electric field and the magnetic film. For comparison, a series of of circular aperture structures was also modeled. These were chosen to have diameters of: 20 nm, to correspond to the width of the cross cavity arms; 40 nm, to correspond to the approximate diameter of the region within which field is confined for a cross cavity; 49 nm, so that the area of the aperture is the same as that of the largest cross; and 160 nm, which is the largest practically achievable aperture within the confines of the modeling geometry. Figure 5 shows the spectral response of the absolute reflected y component of the electric field for the circular apertures together with the 260 nm

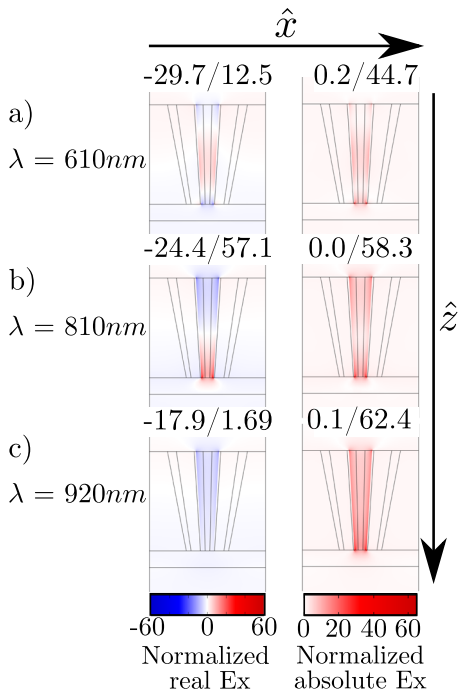

FIG. 4. The distribution of the x component of electric field at the three resonant wavelengths for the 260 nm arm length cross model. The cross-sections show the reflected real (left) and absolute (right) x component of local field, normalized to the incident field amplitude, plotted at one instance in phase. The same colour scale is used for all resonances, and minimum and maximum values of field are shown above the individual field distributions. The distributions are shown for a slice taken through the centre of the model. The orientation is consistent with the schematic shown in Figure 1. In most cases the field is strongly localized at the center of the cross on the dielectric side of the cavity structure.

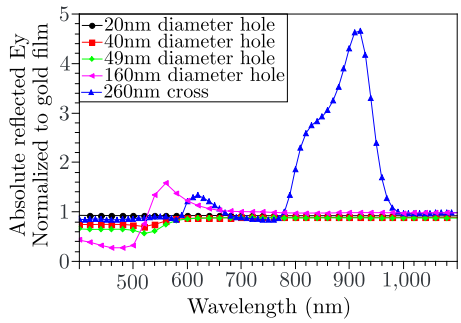

FIG. 5. Dependence of absolute relative *y* component of electric field upon wavelength for a range of small circular apertures together with the 260 nm cross cavity. Spectra have been normalized to that of a continuous gold film.

cross cavity. The cross cavity produces a markedly larger signal than any circular aperture producing comparable field confinement, and a larger signal than the circular aperture of a much larger area. A small wavelength dependent reflected *y* component of electric field was found to occur for models in which the gold film had no defined aperture/cavity. This is most likely an artifact where the imperfect nature of the meshing has introduced an asymmetry that generates the *y* component of electric field. The spectra shown in Figure 5 have therefore been normalized to that obtained from the continuous gold film. The un-normalized spectra are included in the supplementary material SM 1 Figure 1.

The modeling suggests that the absolute MOKE signal may be enhanced by a factor of 2 to 3 at resonance, while E_y is likely to be reduced by a factor of two. This is still a remarkably large signal considering the reduced area of interaction between the electric field and the magnetic film. The cross-shaped cavity is therefore a promising structure for near-field MO sensing that provides an increased signal for a given aperture area when compared to a simple circular aperture. Furthermore, the plasmonic response can be tuned to allow resonance at arbitrary probe beam wavelengths, which is of advantage for use with monochromatic laser sources.

FABRICATION

Any method of realizing the structures explored in the modeling above must take full account of the idiosyncrasies of the fabrication tools available. In principle, the simplest approach is to deposit a multi-layer structure containing the magnetic, dielectric and gold layers and then define the cavity within the gold by subtractive etching or milling. To this end, multi-layer films of composition $Pt(500nm)/4\times\ [Co(0.6nm)/Pt(1.5nm)]/Ta_2O_5(50nm)/Au(xnm)$ were fabricated by UHV co-sputtering. Given that the width of the desired arm features is small compared to the thickness of the gold, focused ion beam (FIB) milling appears well suited to the definition of the cavity structure. However it quickly became apparent that FIB milling was detrimental to the desired MO response, in agreement with previous studies that showed that implantation of a magnetic film with gallium may alter its MO response.[31] A reduction of the MOKE signal was found to occur for any milled structure, while details of unsuccessful attempts to mitigate the signal loss can be found in the supplementary material SM 2. In addition, the cut cross cavity that is of primary interest here has a region at the center of the cross that by necessity is milled twice. The overlapped milling at the center would erode any underlying layer, even if gallium implantation of the remaining material could be eliminated. This is illustrated in Figure 6 where a cross section through a portion of a partially milled cross cavity array shows that the center of each cavity is milled deeper than the arms.

The combination of a loss of MO signal from gallium implantation and overmilling at the centre of the cross, clearly makes top-down monolithic FIB fabrication infeasible. Nevertheless FIB milling remains attractive because it is well suited to the definition of deep, high aspect ratio features, and can be applied to structures of non-planar topography such as the AFM tips used recently for near-field TRSKM. Therefore a related method was employed in which a cross cavity structure could first be

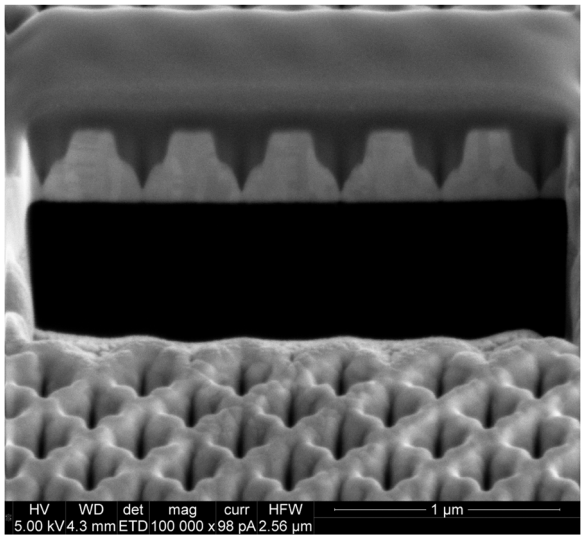

FIG. 6. SEM micrograph of a cross section taken through the center of several partially milled cross cavities. The central region of each cavity is milled to a greater depth due to the overlap of milling in this region.

prepared by FIB milling and then transferred to a different substrate supporting a magnetic film. The process shown in schematic form in Figure 7 is adapted from a method described previously.[32] A sacrificial glass slide is spin-coated with ≈ 450 µL of PSS (Poly(4-styrenesulfonic acid), a water soluble polymer. This polymer is then allowed to cure in air for several hours. After curing the PSS forms a relatively stable base upon which gold may be deposited by magnetron sputtering. The gold coated PSS film is patterned and then placed in a DI water bath to dissolve the PSS layer and allow the gold film to float to the surface of the water. A clean substrate, coated with a $Ta(5nm)/Pt(3nm)/4\times[Co(0.5nm)/Pt(3nm)]/Ta_2O_5(50nm)$ film, is then placed beneath the floating gold film, so that the gold sits on the substrate when water is drained from the bath. By drying in clean air with the substrate held vertical, a combination of gravity and evaporation allows remaining water to be removed, leaving a gold film that is flat but for a few fine creases.

For the structures fabricated by the floating method, 300 nm of gold was deposited onto the dried PSS coated glass slide by means of magnetron sputtering. FIB milling of cross cavity arrays requires careful consideration of the ion beam parameters. High resolution FIB patterning favors a small spot

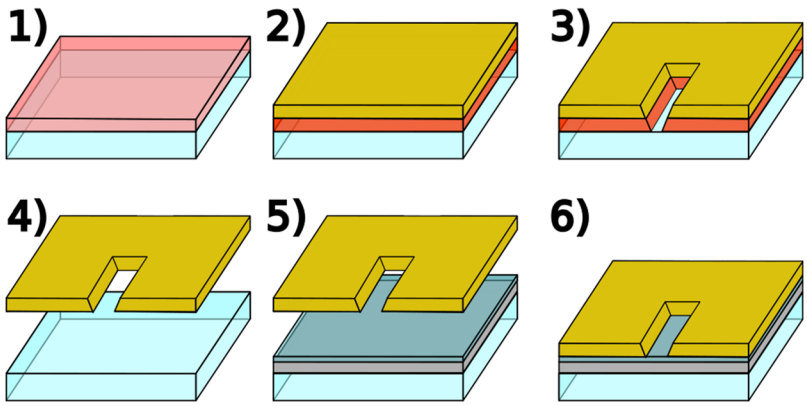

FIG. 7. Schematic of the full float process. 1) PSS is spin coated onto a clean glass slide, and allowed to cure. 2) Gold is deposited onto the dried PSS film. 3) FIB milling is performed upon the gold and PSS layers. 4) The entire film is placed in a de-ionized water bath, and the gold allowed to float to the surface. 5) A new clean substrate with a magnetic film (and dielectric spacer layer) is placed beneath the gold film. 6) The gold film is placed onto the new substrate, and allowed to dry.

size, which in turn favors a low emission current. However lower emission currents require longer milling times, which can lead to distortion related to sample drift (mechanical and thermal drift of the sample stage). A FIB voltage of 30kV and current of 50pA were found to be a good compromise, producing a small spot size (≈20 nm) and acceptable patterning time (1-5 minutes depending on the depth and size of the patterned arrays).

OPTICAL CHARACTERIZATION METHODS

The optical properties of the fabricated structures were characterized by the complementary techniques of transmission micro-spectroscopy and scanning Kerr microscopy. Transmission micro-spectroscopy was used to study the plasmonic properties of the cavity structures immediately after FIB milling, while scanning Kerr microscopy was used to study the MO response of the structures after they had been overlaid on a magnetic film. A schematic of the transmission micro-spectroscopy apparatus is shown in Figure 8. Light source from an extended source is loosely focused by a condenser lens onto the structures from the milled side (as in the modeling outlined previously), and then the transmitted light is collected by an objective lens from the other side. This light was then analyzed by a "Spectrapro 2500i" spectroscope, and the resulting spectrum recorded. Since the PSS layer and glass substrates were optically transparent, the milled structures were characterized by transmission micro-spectroscopy prior to floating of the gold films. A dark count is then subtracted from the resulting spectra, and the spectra are then normalized to spectra obtained through a PSS coated glass film with no gold.

The scanning Kerr microscope used to characterize the MO response of the structures is shown in schematic form in Figure 9. A collimated HeNe (633 nm) laser probe is focused on to the sample at normal incidence by a microscope objective lens with a numerical aperture of 0.60, giving a theoretical diffraction limited spot size of 620 nm. Line scans acquired across a sharp edge feature suggest a somewhat larger spot size on the order of 1 micron (a Lorentzian fit to the first derivative of a line scan yields a FWHM of $0.93\mu m$). The reflected beam is collected by the objective lens, and directed into a detector containing a polarizing beam splitter, and pair of balanced photo-diodes. Through suitable subtraction of the signals from the two photo-diodes, the rotation of the plane of polarization induced by the MOKE can be obtained. The sample is mounted on a piezo-electric stage, allowing imaging of the sample (by raster scanning) and precise positioning of the probe beam on the sample.

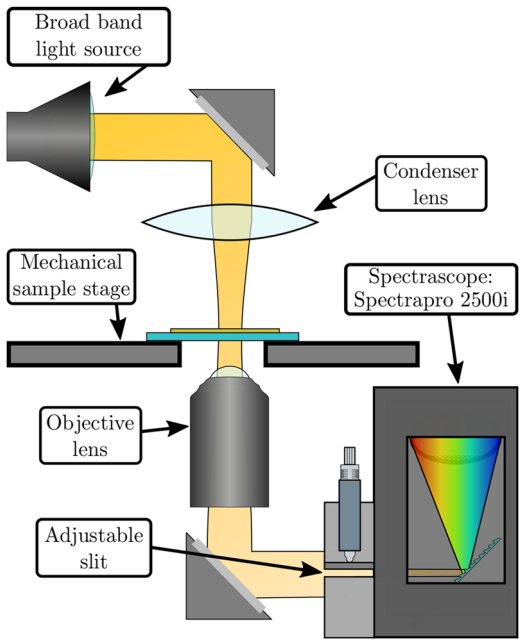

FIG. 8. Schematic of the transmission micro-spectroscope described within the main text.

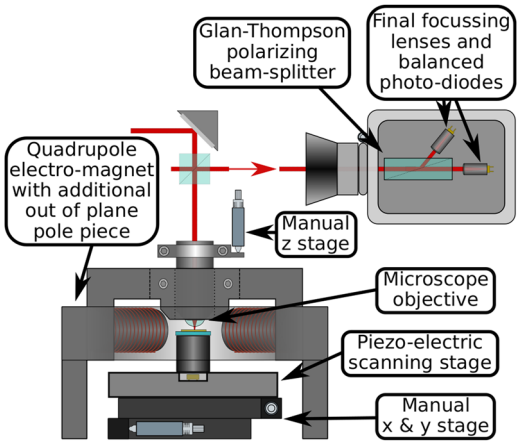

FIG. 9. Schematic of the scanning Kerr microscope described within the main text that is used to record magnetic hysteresis loops.

Coarse position positioning is achieved by mounting the piezo stage upon mechanical translation stages. A quadrupole electro-magnet allows a static magnetic field to be applied in any direction within the plane of the sample, while an out of plane field is obtained through the use of an additional yoke arm and return pole that are situated above the plane of the quadrupole. This additional return pole reduces sample accessibility, and generates a somewhat spatially inhomogeneous field along the optical path. As such calibrations of field, while consistent within a given experimental set, should be taken as approximate. The objective lens is recessed into the return pole and directs light onto the sample through a small hole in the face of the pole piece.

TRANSMISSION SPECTRA OF CROSS ARRAYS

Scanning electron microscope (SEM) images of selected cross arrays fabricated within a gold film deposited on PSS are shown in Figure 10.

Before the gold film was floated onto a magnetic substrate a series of transmission spectra were first acquired. Spectra for cross arrays of varying arm length are shown in Figure 11(a) after subtraction of the detector dark count and normalization to the spectrum of the lamp source (individually plotted versions of these spectra can be found in the supplementary material SM 3 Figure 5). For some spectra three distinct peaks may be seen, and have been labeled in the same manner as the peaks observed in the modeled spectra presented above. Peaks observed at about 600 nm, similar to those observed in the modeling, may be associated with confinement of a half wavelength within the 300nm thickness of the gold film, since they do not appear to shift with changing cross length. For crosses with arm length less than 240 nm the wavelength of the "B" peak appears to increase with arm length, before becoming constant for larger crosses. Finally a third peak can be seen for devices with a cross length greater than 220 nm, and its wavelength again appears to increase with increasing cross length. The experimental spectra are more complicated than the modelled spectra of Figure 2. Consistent fitting was not possible, and peak positions were estimated from the positions at which local minima in the gradient occurred. The positions of the three peaks have been plotted within Figure 11(b) for the cases in which they could be clearly identified, together with the peaks observed in the modeling for ease of comparison. As in the modeling three regimes are observed as the cross length is varied. The observed plateauing of the "B" peak position for cross lengths greater than 220 nm occurs at a wavelength close to 700 nm, which corresponds to the peak of the lamp spectrum. Therefore lamp breakthrough, or imperfect normalization at wavelengths close to 700 nm, may be masking the true spectral response of the cross cavities in this case. The imperfect normalization may be due to several contributing factors. By necessity the lamp spectra is obtained from a non-gold coated region of the PSS coated slide, and due to the limitations of spin coating, this region is likely to have a different thickness of PSS than that of the gold coated region. It is also possible that the light from the lamp may have leaked into the detector causing breakthrough.

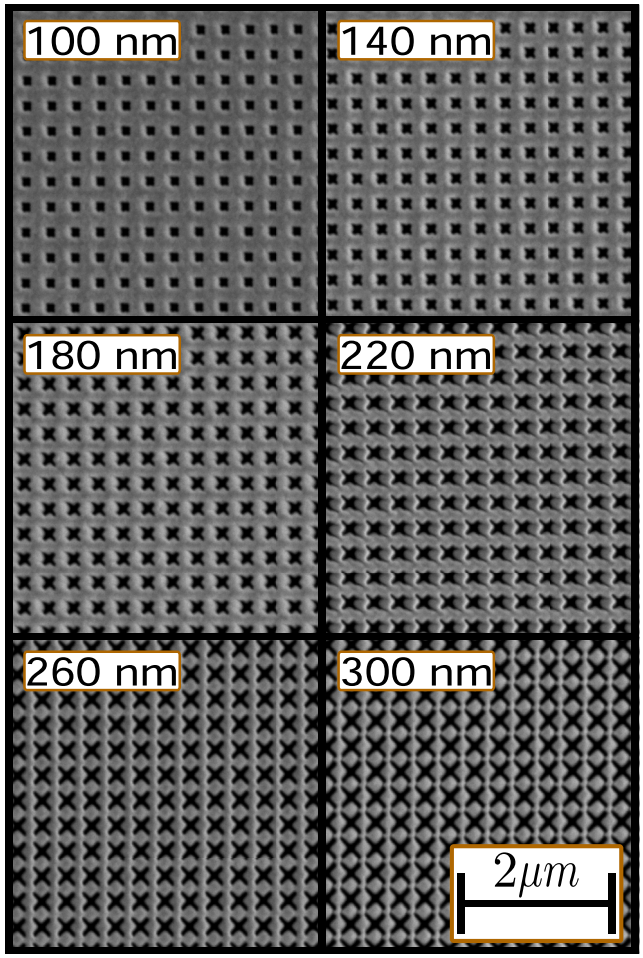

FIG. 10. SEM micrograph of cross arrays with arm lengths in the range of 100 nm to 300 nm.

It should be noted that direct comparison between modeling and experiment is complicated by two factors. Firstly, there is some ambiguity in the stated arm lengths. The mean cross length is used for the modeled structures, while cross length specified in the patterning file is used for the experimental structures. The cross sectional detail of the crosses, i.e. the slope and curvature, are difficult to parameterize. This makes it likely that the geometry of the fabricated and modeled structures is different in detail. Secondly the nature of the region beneath the gold film differs between the modeled and experimental systems. The modeled system was designed to mimic a successfully floated gold film, with a thin dielectric spacer between the gold and an underlying magnetic layer. However in the experiment the gold film is supported by a thicker PSS layer deposited on a glass substrate. Accurately modeling the PSS layer is complicated by variations in the thickness of the PSS film between fabricated samples (that arise due to the non-uniform thickness of the spin coated PSS), and difficulty in characterizing the optical properties of dried PSS. Despite some quantitative differences in the spectra between modeled and fabricated crosses, the broad trends are similar. In both cases resonances in the visible and near infra-red are observed, the resonant wavelengths appear to scale linearly with cross arm length, and a transition between two regimes seems to occur in both cases.

RESULTS OF SCANNING KERR MEASUREMENTS

In addition to cross-arrays, a series of isolated circular test apertures with diameter in the range 300 nm to 4μm were also fabricated within the gold film prior to floating. As such the diameters

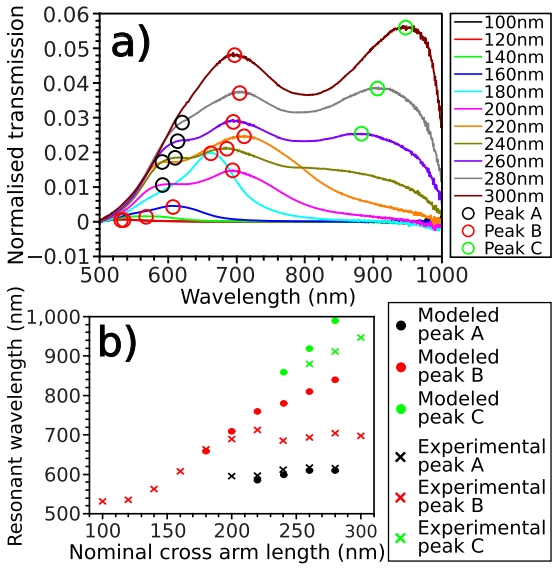

FIG. 11. a) Transmission spectra obtained from cross array structures of different arm length defined within a 300 nm thick gold film, prior to floating. b) Peak wavelength is plotted against nominal arm length for the observed peaks. The modeled results shown in Figure 2, are included for comparison. The stated arm lengths are the mean arm length for the modeled spectra, and the arm length from the patterning file for experimental spectra.

ranges from the sub-wavelength regime to larger than the spot size of about 1 μm. SEM images of these structures are presented in the supplementary material SM 3 Figure 6. Representative MOKE hysteresis loops obtained from the circular apertures are shown in Figure 12, with the full set presented in the supplementary material SM 3 Figure 7. The circular apertures exhibited clear MOKE hysteresis loops when the diameter was larger than that of the focused probe beam. Some sub-wavelength apertures also showed clear hysteresis loops of reduced height. However some apertures within the set exhibited either no loop or loops of significantly reduced height. It should be noted that calibration

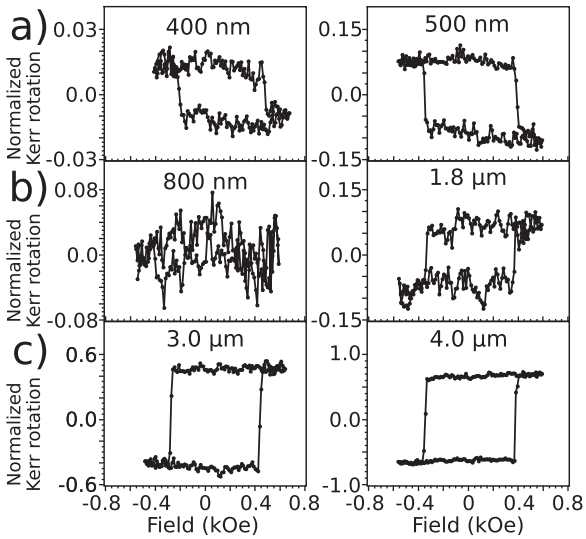

FIG. 12. MOKE hysteresis loops obtained from circular apertures of different diameter defined within a floated gold film. Due to the difficulty in calibrating the absolute Kerr rotation in this regime, all data has been normalized to the sample reflectivity. a) Loops acquired from apertures of sub-wavelength diameter showing a significant but reduced Kerr signal. b) Loops from apertures of intermediate diameter. c) Loops from apertures with diameter considerably larger than the spot size.

of the Kerr rotation requires a substrate for which the reflectivity is reasonably consistent across the region being probed. For measurements of apertures with diameter smaller then the probe beam, this is no longer the case, with gold regions and exposed magnetic regions being sampled simultaneously. Small variations in the position of the probe spot can produce artificially large changes in the apparent Kerr rotation. Therefore all of the Kerr rotation signals presented in Figure 12 have been normalized to the reflectivity signal that was measured simultaneously.

Having established the feasibility of MOKE measurements through floated FIB milled structures, attempts were made to obtain MOKE hysteresis loops from cross cavity structures. For the He:Ne laser wavelength of 633 nm, crosses with arm lengths between 130 nm and 150 nm should be promising candidates for the observation of enhanced Kerr signal. However no Kerr signal was observed for any of the cross structure arrays, from multiple device sets, fabricated in a number of different gold films. FIB milling was therefore used to cut a rectangular flap around three sides of an array that happened to sit on a crease in the gold film. The flap was observed to open of its own accord due to electrostatic charging, allowing the underside of the flap to be observed by SEM. This revealed an array of nanotubes adhering to the underside of the milled gold as shown in Figure 13. Further cross-sectioning of other array structures revealed the presence of nanotubes in all cases studied. The nanotubes have a bright and ragged edge, with some bright flecks as can be seen in Figure 13(d) suggesting possible metallic implantation. This suggests that the capillaries may be formed by deposition of gallium, or re-deposition of gold, reinforcing the PSS in the milled regions. In addition it is possible that the FIB beam alters the structure of the PSS and so reduces its local solubility.

The variation in the value of the saturation Kerr rotation within the observed MOKE loops from apertures may now be understood in terms of the tendency for tube structures to adhere to isolated apertures of different diameter. For sufficiently large diameters ($>\approx 3\mu m$) either the tube does not adhere, or does not prevent the optical field reaching the magnetic film through the aperture, so as to produce a strong MOKE signal. For the smallest diameters, the larger aspect ratio (length to diameter) of the nanotube makes an isolated nanotube easier to dislodge, so that the gold surrounding the aperture comes into direct contact with the dielectric layer, allowing its near field to interact with the magnetic film beneath the dielectric. On the other hand, for apertures of intermediate diameter,

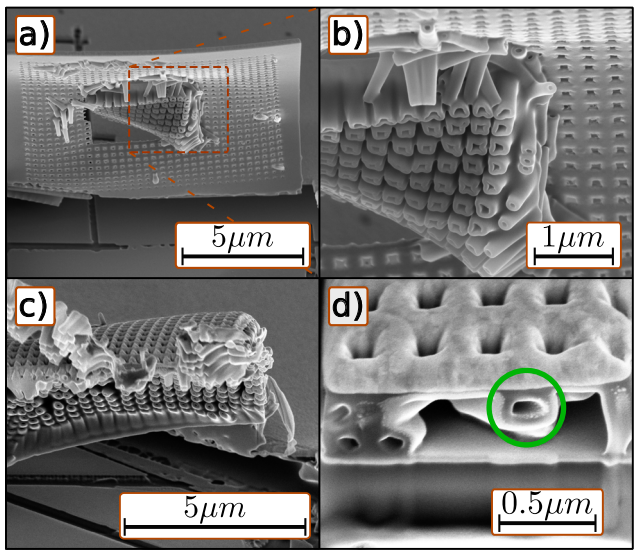

FIG. 13. SEM micrographs of nanotube structures under cross arrays. a) A flap within a cross array that has been cut and lifted through FIB milling. A large cluster of nanotubes is seen within the center of the flap. b) A higher magnification image of the central cluster seen in a). Some of the nanotubes have collapsed, while some seem to have a cross shaped profile. c) Another flap within a cross array that has curled during the lifting process. Here the nanotubes appear to be more uniformly distributed. d) A cross section through a cross array that refused to lift, showing collapsed nanotubes beneath the gold, a region of possible metallic implantation is shown in green.

the tube is more likely to remain attached and prevent the near field of the aperture reaching the magnetic layer. Alternatively, if the aperture diameter is sufficiently large as to permit transmission into the far field with the nanotube attached, most of the radiation that reaches the magnetic layer is multiply reflected, and dissipated between the magnetic layer and the gold, so that the measured Kerr rotation is suppressed. The successful recovery of MOKE hysteresis loops from isolated sub-wavelength apertures engenders confidence that the gold float process is in principle a feasible approach. There may be scope for preventing the adhesion of nanotubes to the floated gold film either by modification of the milling pattern, changes to the float process, or use of an alternative soluble layer.

CONCLUSION

A suitably structured plasmonic cavity structure has great potential for use as a near field MO imaging probe capable of enhancing a MOKE signal while improving spatial resolution of the measurement system by bypassing the diffraction limit. Cross shaped cavities were thought to be a promising candidate for magneto-optical probes, since they possess four fold symmetry, can be tuned to a specific laser wavelength, and strongly confine the area of interaction with the sample. Finite element modeling of such structures interacting with a magnetic layer showed clear tunable enhancement of the MOKE signal, with large MOKE signal at resonance despite a sizeable reduction of the area of interaction. The resonant properties of such cavities have been observed in transmission spectra, supporting the validity of the modeling. However initial monolithic fabrication of such structures by FIB milling suffered from poisoning of the magnetic layer due to gallium implantation and overmilling of the underlying structure at the center of the cross. As such a gold floating technique was developed that overcame this issue, allowing recovery of a full MOKE signal from circular apertures of few micron diameter. However this technique was found to be unsuitable for the structures of primary interest (cut-cross cavities) due to formation of nanotube structures underneath the patterned regions of the gold film. The nanotubes remain attached to the gold during the float process and methods for their removal are currently being investigated. In spite of these difficulties, recovery of a strong magneto-optical signal from sub-wavelength apertures in a floated gold film has been demonstrated. Further refinement of the gold float process will allow fabrication of hybrid plasmonic/magnetic structures. Integration of cross shaped cavities with the existing near field magneto-optical scanning microscope outlined in Ref. 10, would allow for MO imaging with sub-wavelength spatial resolution and sub pico-second time resolution. This work has broad implications for both the fabrication of a range of magneto-optically active structures, and the characterization of static and dynamic magnetic properties at the nano scale.

SUPPLEMENTARY MATERIAL

See supplementary material for a more detailed exploration of the effects of gallium poisoning on magneto-optical signal, as well as material underpinning various figures presented in this manuscript.

ACKNOWLEDGMENTS

Financial support from the UK Engineering and Physical Science Research Council (EPSRC) grants EP/1038470/I and EP/1038411/1 is gratefully acknowledged. We also acknowledge the support of Seagate Technology (Ireland) under SOW 00077300.0. RMB contribution to project was supported by the Royal Academy of Engineering under the Research Chairs and Senior Research Fellowships Scheme.

APPENDIX : SOFTWARE AND DATA AVAILABILITY

The research materials supporting this publication can be publicly accessed in the open research Exeter (ORE) repository via the following persistent identifier: https://doi.org/10.24378/exe.309

[1] R. J. Hicken, Philosophical Transactions of the Royal Society of London A: Mathematical, Physical and Engineering Sciences **361**, 2827 (2003).
[2] C. Chappert, A. Fert, and F. N. D. Dau, Nature Materials **6**, 813 (2007).
[3] S. Pizzini, J. Vogel, M. Bonfim, and A. Fontaine, "Time-resolved x-ray magnetic circular dichroism: A selective probe of magnetization dynamics on nanosecond timescales," in *Spin Dynamics in Confined Magnetic Structures II*, edited by B. Hillebrands and K. Ounadjela (Springer Berlin Heidelberg, Berlin, Heidelberg, 2003), pp. 157–187.
[4] C. Stamm, Physical Review B: Condensed Matter and Materials Physics **86** (2012).
[5] D. Neeb, A. Krasyuk, A. Oelsner, S. A. Nepijko, H. J. Elmers, A. Kuksov, C. M. Schneider, and G. Schönhense, Journal of Physics: Condensed Matter **17**, S1381 (2005).
[6] N. Bukin, C. McKeever, E. Burgos-Parra, P. S. Keatley, R. J. Hicken, F. Y. Ogrin, G. Beutier, M. Dupraz, H. Popescu, N. Jaouen, F. Yakhou-Harris, S. A. Cavill, and G. van der Laan, Scientific Reports **6**, 36307 (2016).
[7] W. Yu, P. S. Keatley, P. Gangmei, M. K. Marcham, T. H. J. Loughran, R. J. Hicken, S. A. Cavill, G. van der Laan, J. R. Childress, and J. A. Katine, Physical Review B **91**, 174425 (2015).
[8] R. A. J. Valkass, W. Yu, L. R. Shelford, P. S. Keatley, T. H. J. Loughran, R. J. Hicken, S. A. Cavill, G. van der Laan, S. S. Dhesi, M. A. Bashir, M. A. Gubbins, P. J. Czoschke, and R. Lopusnik, Applied Physics Letters **106**, 232404 (2015).
[9] P. S. Keatley, V. V. Kruglyak, R. J. Hicken, J. R. Childress, and J. Katine, Journal of Magnetism and Magnetic Materials **306**, 298 (2006).
[10] P. S. Keatley, T. H. J. Loughran, E. Hendry, W. L. Barnes, R. J. Hicken, J. R. Childress, and J. A. Katine, Review of Scientific Instruments **88**, 123708 (2017).
[11] D. K. Gramotnev and S. I. Bozhevolnyi, Nature Photonics **4**, 83 (2010).
[12] T. W. Ebbesen, H. J. Lezec, T. Ghaemi, and P. A. Wolff, Nature **391**, 667 (1998).
[13] S. Carretero-Palacios, O. Mahboub, F. J. Garcia-Vidal, L. Martin-Moreno, S. G. Rodrigo, C. Genet, and T. W. Ebbesen, Optics Express **18** (2011).
[14] C. Genet and T. W. Ebbesen, Nature **445**, 39 (2007).
[15] O. Mahboub, S. Carretero-Palacios, C. Genet, F. J. Garcia-Vidal, S. G. Rodrigo, L. Martin-Moreno, and T. W. Ebbesen, Optics Express **18** (2010).
[16] N. Maccaferri, J. B. González-Díaz, S. Bonetti, A. Berger, M. Kataja, S. van Dijken, J. Nogués, V. Bonanni, Z. Pirzadeh, A. Dmitriev, J. Åkerman, and P. Vavassori, Optics Express **21**, 9875 (2013).
[17] N. Maccaferri, A. Berger, S. Bonetti, V. Bonanni, M. Kataja, Q. H. Qin, S. van Dijken, Z. Pirzadeh, A. Dmitriev, J. Nogués, J. Åkerman, and P. Vavassori, Physical Review Letters **111**, 167401 (2013).
[18] N. Maccaferri, K. E. Gregorczyk, T. V. A. G. de Oliveira, M. Kataja, S. van Dijken, Z. Pirzadeh, A. Dmitriev, J. Åkerman, M. Knez, and P. Vavassori, Nature Communications **6**, 6150 (2015).
[19] A. Berger, R. Alcaraz de la Osa, A. K. Suszka, M. Pancaldi, J. M. Saiz, F. Moreno, H. P. Oepen, and P. Vavassori, Physical Review Letters **115**, 187403 (2015).
[20] P. K. Jain, Y. Xiao, R. Walsworth, and A. E. Cohen, Nano Letters **9**, 1644 (2009).
[21] J. B. González-Díaz, A. García-Martín, J. M. García-Martín, A. Cebollada, G. Armelles, B. Sepúlveda, Y. Alaverdyan, and M. Käll, Small **4**, 202 (2008).
[22] G. Armelles, J. B. González-Díaz, A. García-Martín, J. M. García-Martín, A. Cebollada, M. U. González, S. Acimovic, J. Cesario, R. Quidant, and G. Badenes, Optics Express **16**, 16104 (2008).
[23] T. H. J. Loughran, P. S. Keatley, E. Hendry, W. L. Barnes, and R. J. Hicken, Optics Express **26**, 4738 (2018).
[24] A. Hubert and R. Schäfer, *Chap. Domain Observation Techniques* (Springer, 1998).
[25] Q. Qiu and S. D. Bader, Review of Scientific Instruments **71**, 1243 (2000).
[26] G. Neuber, R. Rauer, J. Kunze, T. Korn, C. Pels, G. Meier, U. Merkt, J. Bäckström, and M. Rübhausen, Applied Physics Letters **83**, 4509 (2003).
[27] P. B. Johnson and R. W. Christy, Physical Review B: Condensed Matter and Materials Physics **6**, 4370 (1972).
[28] B. Sepúlveda, J. B. González-Díaz, A. García-Martín, L. M. Lechuga, and G. Armelles, Physical Review Letters **104**, 147401 (2010).
[29] B. Caballero, A. Garcia-Martin, and J. Cuevos Carlos, ACS Photonics **3** (2016).
[30] M. Mansuripur, *The physical principles of magneto-optical recording* (Cambridge University Press, 1995).
[31] J. Gierak, E. Bourhis, G. Faini, G. Patriarche, A. Madouri, R. Jede, L. Bruchhaus, S. Bauerdick, B. Schiedt, A. Biance, and L. Auvray, Ultramicroscopy **109**, 457 (2009).
[32] F. Min Huang, J. K. Sinha, N. Gibbons, P. N. Bartlett, and J. J. Baumberg, Applied Physics Letters **100**, 193107 (2012).